Lasing modes in polycrystalline and amorphous photonic structures

Jin-Kyu Yang, Heeso Noh, Seng Fatt Liew, Michael J. Rooks, Glenn S. Solomon, and Hui Cao

Phys. Rev. A **84**, 033820 — Published 15 September 2011

DOI: 10.1103/PhysRevA.84.033820

Lasing modes in Polycrystalline and Amorphous Photonic Structures

Jin-Kyu Yang[1,2], Heeso Noh[1], Seng Fatt Liew[1], Michael J. Rooks[1], Glenn S. Solomon[3], Hui Cao[1,4]
[1] *Department of Applied Physics, Yale University, New Haven, CT 06520*
[2] *Department of Optical Engineering, Kongju National University, Kongju 314-701, Republic of Korea*
[3] *Joint Quantum Institute, NIST and University of Maryland, Gaithersburg, MD 20899*
[4] *Department of Physics, Yale University, New Haven, CT 06520*
(Dated: August 19, 2011)

We systematically studied the lasing characteristics in photonic polycrystalline and amorphous structures. 2D arrays of air holes were fabricated in a GaAs membrane. InAs quantum dots embedded in the membrane provide gain for lasing under optical pumping. The lasing modes are spatially localized, and blue-shift as the structural order becomes shorter-ranged. Our three-dimensional numerical simulations reveal that the out-of-plane leakage of the lasing mode dominates over the in-plane leakage. The lasing modes in a photonic polycrystalline move away from the center frequency of the photonic band gap to reduce the out-of-plane leakage. In a photonic amorphous structure, the short-range order improves optical confinement and enhances the quality factor of resonances. Understanding the behavior of photonic polycrystalline laser and amorphous laser opens the possibility of controlling lasing characteristic by varying the degree of structural order.

I. INTRODUCTION

Periodic modulation of refractive indices in photonic crystals (PhCs) result in the formation of photonic bandgaps (PBGs) within which light propagation is prohibited[1–3]. One important application of PhC is the low-threshold laser. The distributed feedback PhC laser relies on the slow group velocity at a photonic bandedge to enhance light amplification[4]. The PhC defect mode laser utilizes light localization at a structural defect to minimize the lasing threshold[5,6]. In addition to PhCs, lasing action in photonic quasi-crystals with and without defects has been reported[7–11]. Despite lack of periodicity, the quasi-crystalline photonic structure has long-range orientational order and can possess a PBG. An amorphous photonic system has neither long-range translational order nor orientational order. However, the density of optical states (DOS) may be depleted through coupled Mie resonances[12–17] or short-range structural order[18,19]. Recently the transition from photonic polycrystalline to amorphous structures was mapped out via a gradual change of the domain size[20]. In a photonic polycrystal the PBG is formed within each domain of periodic structure, while in an amorphous structure the domains are too small to have a significant PBG. Despite the absence of a PBG in an amorphous structure, optical confinement is improved by the short-range order, leading to more efficient lasing[21]. However, there has been no systematic study on lasing characteristic in polycrystalline and amorphous structures. What determines the lasing frequencies, what is the nature of lasing modes, and how different is a polycrystalline laser from an amorphous laser? Answering the above questions will provide a physical insight to lasing mechanism in photonic structures lacking long-range order.

This paper presents experimental and numerical studies on lasing in polycrystalline and amorphous photonic structures. We fabricated two-dimensional (2D) arrays of air holes in a free-standing GaAs membrane. InAs quantum dots were embedded in the membrane and provide gain under optical pumping. We realized lasing in photonic polycrystalline and amorphous structures. The lasing modes display a systematic shift in frequency as the short-range order changes. Our 2D numerical simulations predict that the modes with the highest quality (Q) factor and the lowest lasing threshold are found at the center frequency of the original PBG. This prediction contradicts the experimental observation of lasing frequency shift, because light leakage in the third dimension was ignored. Our 3D calculations illustrate that light leakage out of the plane of membrane dramatically reduces the Q factor of strongly localized modes near the PBG center. Consequently the lasing modes in photonic polycrystalline move away from the PBG center in order to avoid the large vertical leakage. In an amorphous photonic structure, however, the lasing modes are less localized since the PBG effect becomes weak. The vertical leakage is weaker, and the lasing modes do not shift in frequency.

The article is organized as follows. Section II describes the fabrication of photonic polycrystalline and amorphous structures, and experimental characterization of lasing in these structures. In section III, results of 2D and 3D numerical calculations of high-Q modes and DOS are presented. Finally we conclude in section V.

II. SAMPLE FABRICATION AND LASING EXPERIMENT

Polycrystalline and amorphous arrays of cylinders were created in a computer simulation with a jammed packing protocol[20]. A detailed description of structure generation and characterization can be found in ref[20]. Briefly, polydisperse cylinders were jam-packed to preserve short-range order, then the diameters of all cylinders were reduced to a constant value. The final configurations have disorder only in the position of cylinders. By changing the initial polydispersity of cylinders, we were able to vary the degree of position disorder over a wide range. Our previous study of DOS in these structures[20] demonstrated that the polycrystalline and amorphous regimes can be identified by comparing the average domain size to the Bragg length (attenuation length of Bragg scattering).

The computer generated patterns were transferred to a GaAs membrane. A 190-nm-thick GaAs layer and a 1000-nm thick $Al_{0.75}Ga_{0.25}As$ layer were grown on a GaAs substrate by molecular beam epitaxy. Inside the GaAs layer there were three uncoupled layers of InAs QDs equally spaced by 25 nm GaAs barriers. 2D arrays of cylinders were written on a 300-nm-thick ZEP layer with the electron-beam lithography. The patterns were transferred to the GaAs layer by chlorine-based inductive-coupled-plasma reactive-ion-etching with the ZEP layer as a mask. The ZEP layer was subsequently removed in an oxygen plasma cleaning process. Finally the $Al_{0.75}Ga_{0.25}As$ layer was selectively removed by a dilute HF solution. Figure 1(a,b) shows the top-view scanning electron microscope (SEM) images of two fabricated patterns. The lateral dimension of a pattern is 9.3 μm, and it has 1024 air holes. The radius of air holes r is 100 nm. In the pattern of Fig. 1(a), we can clearly see domains of the triangular lattice of holes, each domain has a different orientation. In Fig. 1(b), the domains are so small that barely visible.

For qualitative understanding of the short-range order, the 2D spatial correlation function $C(\Delta\mathbf{r})$ for these patterns were calculated. A typical ensemble-averaged $C(\Delta\mathbf{r})$ is presented in Fig. 1(c). It consists of rings whose amplitudes decrease with increasing spatial separation $\Delta r \equiv |\Delta\mathbf{r}|$. Since $C(\Delta\mathbf{r})$ is isotropic, we calculated the azimuthal-averaged $C(\Delta r)$ for the two patterns in (a,b) and plotted the peak amplitudes in Fig. 1(d). The first peak away from $\Delta r = 0$

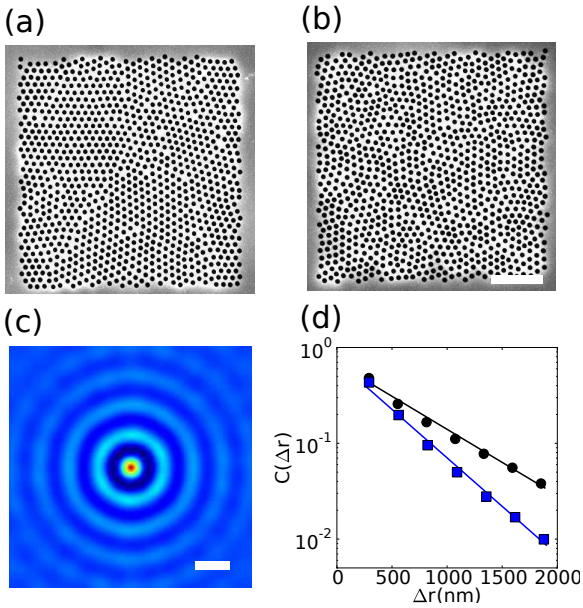

FIG. 1. (Color online)(a,b) top-view SEM images of fabricated arrays of air holes in a GaAs membrane. The scale bar is 2 μm. Ordered domains of different orientations can be seen in (a), but barely in (b). (c) 2D spatial correlation function $C(\Delta\mathbf{r})$ averaged over five configurations including the pattern in (b) and equivalent ones. Scale bar = 300 nm. (d) log-linear plot of the peak amplitude of azimuthal-averaged spatial correlation function $C(\Delta r)$, squares for the pattern in (a), and circles for (b). The straight lines are exponential fit , giving the decay length $\xi = 2.3$a for (a) and 1.4a for (b).

is produced by the nearest cylinder, thus its position corresponds to the average spacing a of the nearest neighbors. The two patterns in Fig. 1(a,b) have $a = 290$ nm. The faster damping of $C(\Delta r)$ for the pattern in Fig. 1(b) reflects the spatial correlation is shorter-ranged. They both fall on straight lines in a log-linear plot, indicating exponential decays. The decay length $\xi = 2.3a$, and $1.4a$ for the patterns in Fig. 1(a,b). According to our previous study[20] and the calculation results in the next section, the pattern in Fig. 1(a) is polycrystalline and (b) amorphous.

In the lasing experiments, the samples were cooled to 10 K in a continuous-flow liquid Helium cryostat, and optically pumped by a mode-locked Ti:Sapphire laser (pulse width $\sim$ 200 fs, center wavelength $\sim$ 790 nm, and pulse repetition rate $\sim$ 76 MHz). A long working distance objective lens (numerical aperture = 0.4) focused the pump light to a pattern at normal incidence. The diameter of pump spot on the sample surface was about 2 μm. The emission from the sample was collected by the same objective lens. The emission spectrum was measured by a half-meter spectrometer with a liquid-nitrogen-cooled coupled-charged-device (CCD) array detector. Simultaneously the spatial distribution of emission intensity across the sample surface was projected onto a thermoelectric-cooled CCD camera.

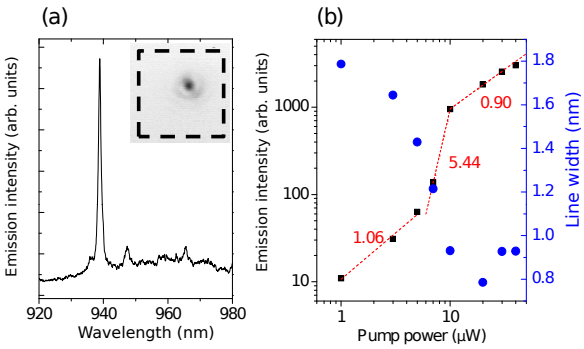

FIG. 2. (Color online)(a) Measured spectrum of emission from a pattern of $\xi = 4.4a$ and $a = 290$ nm at the incident pump power $P = 30$ μW. The inset is an optical image of the lasing mode corresponding to the sharp peak in the emission spectrum. Black dashed square marks the pattern boundary. (b) Intensity I (black square) and width $\Delta\lambda$ (blue circle) of the lasing peak in (a) versus the incident pump power P in a logarithmic plot. The red dotted lines represent linear fit of $\log I$ vs. $\log P$ in three regimes, and the numbers next to them are those slopes.

Figure 2(a) is part of a time-integrated spectrum of emission from a polycrystalline pattern ($\xi/a = 4.4$, $a = 290$ nm). It features a sharp peak on top of a broad QD emission band. Figure 2(b) plots the intensity I and linewidth $\Delta\lambda$ of this peak as a function of the incident pump power P. The variation of $\log I$ with $\log P$ exhibits a S-shape with two kinks. The slopes in the three regimes separated by the two kinks were obtained from curve fitting and written on the graph. In the first and last regimes, the slopes of $\log I$ over $\log P$ are very close to unity, indicating a linear growth of I with P. The second regime has a slope of 5.44, meaning I scales as $P^{5.44}$. The first regime corresponds to spontaneous emission of QDs to a resonant mode, thus the intensity increases linearly with the pump power. When the pump is high enough, the emission peak grows superlinearly as a result of light amplification by stimulated emission. This is the second regime. In the third regime, lasing occurs in this mode, and the gain saturation reduces the slope to one. Also seen in Fig. 2(b), the spectral width $\Delta\lambda$ of the peak first drops quickly with increasing P, then levels off and increases slightly at higher P. The rapid decrease of $\Delta\lambda$ is expected at the onset of lasing oscillation. The gradual increase above the lasing threshold results from the hot carrier effect. Due to the short pulse pumping, the carrier density keeps changing in time. It causes a temporal change of the refractive index, and consequently a continuous red-shift of lasing frequency[22,23]. In our time-integrated measurement of lasing spectrum, the transient frequency shift results in a broadening of the lasing line. Such broadening increases with the hot carrier density and becomes dominant at high pumping level. The inset of Fig. 2(a) is an optical image of the lasing mode, revealing its strong localization inside the pattern whose boundary is marked by the black dashed line.

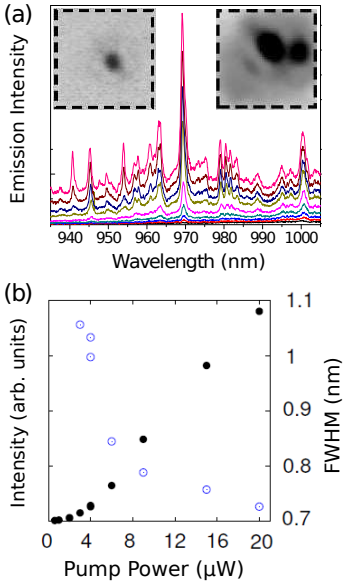

FIG. 3. (Color online)(a) Evolution of emission spectra of a pattern with $\xi/a = 1.4$ and $a = 270$ nm as the pump power increases (from bottom to top). Inset is an optical image of the lasing mode at $\lambda = 970$ nm. (b) Intensity and width of the emission peak at $\lambda = 970$ nm as a function of the pump power.

We also realized lasing in photonic amorphous structures. As seen in Fig. 3(a), there are many peaks of comparable height in the emission spectra of a pattern with $\xi = 1.4a$. Figure 3(b) is a plot of the intensity and width of an emission peak at $\lambda = 970$ nm versus the pump power. The rapid increase of peak intensity and dramatic reduction of the peak width illustrates the onset of lasing action. A tunable interference filter was placed in front of the CCD camera to select this lasing mode for imaging. Inset of Fig. 3(a) are the optical images of two lasing modes. The left one is spatially localized inside the pattern whose boundary was drawn by the dashed line. The double-peaked intensity distribution of the mode on the right is similar to that of a 2D necklace state in[25], suggesting it is a hybrid of two localized states. Further study is needed to confirm it is a necklace state[24,25].

As we moved the pump beam spot across a pattern, new lasing peaks replaced the existing ones, and they have distinct frequencies. This phenomena indicate that resonant modes are localized in different positions of the samples, and brought to lasing when overlapped with the pump spot. We repeated the lasing experiment on several patterns with different arrangement of air holes but same ξ/a, and found the lasing peaks varied from pattern to pattern. We measured the patterns of different ξ/a and recorded the lasing wavelengths. Figure 4 plots the wavelengths of lasing peaks for five values of ξ/a. For a fixed ξ/a, there is a wide spread of lasing wavelengths due to the broad QD gain spectra. Nevertheless, it is evident that the lasing peaks shift to shorter wavelength as the average domain size ξ decreases.

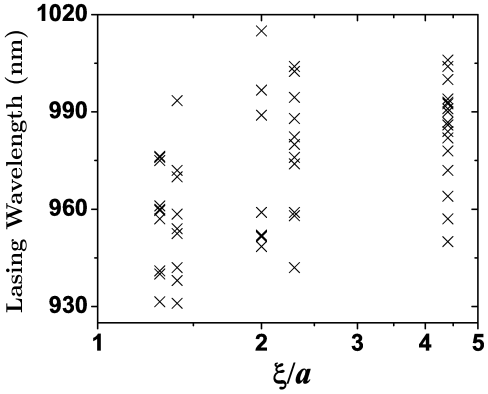

FIG. 4. Measured wavelengths of lasing peaks for patterns of different domain size ξ. The average spacing of nearest-neighboring air holes is a = 290 nm.

III. NUMERICAL SIMULATION OF LASING MODES

To explore the nature of lasing modes in photonic polycrystalline and amorphous structures, we performed numerical simulation. The perforated GaAs membrane is approximated as a 2D array of infinitely long air cylinders embedded in a uniform dielectric host with an effective index of refraction n_w. The value of n_w was obtained in the following steps. First we calculated the photonic band structure of a triangle lattice of air holes in a free-standing GaAs membrane of thickness 190 nm using the plane wave expansion method[26]. The density and size of air holes were identical to those of the fabricated samples. Next we calculated the photonic band structure of the approximate 2D system with n_w as a parameter. By adjusting the value of n_w, we matched the center frequency of the fundamental PBG obtained in the above two cases. In our calculation, we considered only the transverse-electric (TE) polarization (electric field perpendicular to the air cylinder axis), because experimentally the laser emission is TE polarized due to stronger gain of the InAs QDs for the TE polarized light.

Using the finite-difference frequency-domain (FDFD) method, we calculated the resonant modes with long lifetime in the passive structures. Due to the finite size of a pattern, light may escape through the open boundary. The outgoing wave is absorbed by the perfectly matched layer that surrounds the pattern. The resonant modes have finite lifetime, and their frequencies are complex numbers $\omega_r + i\omega_i$. The magnitude of ω_i is inversely proportional to the mode lifetime. The quality factor is defined as $Q = \omega_r/2\,|\omega_i|$. We calculated the complex frequencies of TE modes, and found the highest quality factor Q_m within small frequency bins. Figure 5(a) plots Q_m versus the normalized frequency a/λ for ξ/a = 2.3 and 1.4. Q_m drops quickly as ξ/a decreases. Nevertheless, it reaches the maximum at the same frequency $a/\lambda = 0.3$ for different ξ/a. This result can be explained by the DOS shown in Fig. 5(b). For ξ/a = 2.3, there is a significant depletion of DOS, almost comparable to that of a PhC. The system can be regarded as a photonic polycrystal, as individual domains are large enough to form the PBG via Bragg scattering. Defect modes are formed inside the PBG. The closer their frequencies to the center of PBG, the higher their quality factors. Therefore, the highest-Q resonances in the photonic polycrystal are defect modes. They are strongly localized in space, as can be seen from a typical mode profile in Fig. 5(c). The mode size, computed from the inverse participation ratio of the field disbribution, is about 0.6 μm. When ξ/a is reduced to 1.4, Bragg scattering from each domain is not enough to produce a PBG. Consequently, the DOS has a dip instead of a gap. In this photonic amorphous structure, the

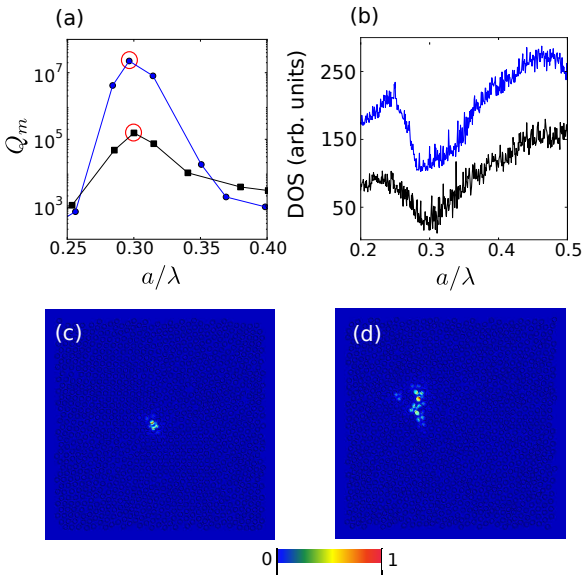

FIG. 5. (Color online)(a) FDFD calculation of approximate 2D structures ($n_w = 2.73$) giving the maximal quality factor Q_m versus the normalized frequency a/λ for $\xi/a = 2.3$ (blue circle) and 1.4 (black square). (b) Calculated DOS for $\xi/a = 2.3$ (top) and 1.4 (bottom). The curves are shift vertically for clarification. Calculated spatial intensity distribution of the highest-Q_m mode for $\xi/a = 2.3$ (c) and 1.4 (d). They are marked with circles in (a).

peak of Q_m coincides with the dip of DOS. The reduction in DOS results from the short-range order, which enhances optical confinement and produces the maximum of Q_m[20,21]. It leads to the maximum of Q_m. The spatial profile of a typical high-Q resonance is shown in Fig. 5(d). The mode size is about 1.0 μm, much smaller than the lateral size of the structure (9.3 μm). This means the mode is still localized spatially, but the degree of localization is less than the defect mode in a polycrystal [Fig. 5(c)]. The maximal Q_m drops quickly as the average domain size ξ decreases.

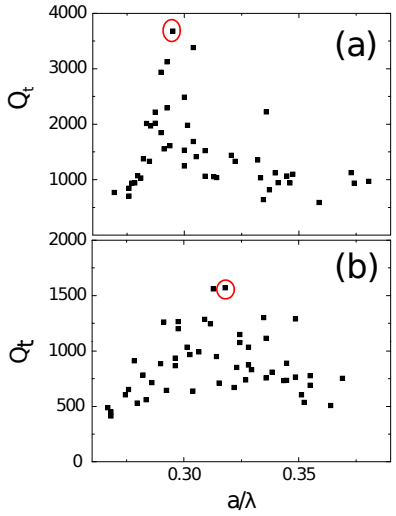

FIG. 6. (Color online)3D FDTD calculation of resonances in the perforated GaAs membrane giving their quality factor Q_t as a function of the normalized frequency a/λ for $\xi/a = 2.3$ (a) and 1.4 (b).

In our experiment the optical gain is distributed nonuniformly across the sample, because the pump spot diameter (~ 2 μm) is smaller than the lateral dimension of the pattern (9.2 μm). Only the QDs inside the pump area are excited and provide optical gain. When light scattering is weak, the lasing modes may be very different from the resonant modes of the passive systems[27,29,30]. However, our samples have strong scattering, the transport mean free path is estimated[28] at $a/\lambda = 0.30$ to be 0.36 μm in the polycrstalline sample ($\xi/a = 2.3$) and 0.53 μm in the amorphous structure ($\xi/a = 1.4$). We extracted the localization length ξ_L in these structures by placing a monochromatic source

at the center and calculating the steady-state field distribution. From the decay of the field intensity away from the source, we get $\xi_L = 0.38$ μm at $a/\lambda = 0.30$ in the sample of $\xi/a = 2.3$, and 0.46 μm in the sample of $\xi/a = 1.4$. Since the localization length is much smaller than the system size, the resonant modes are strongly confined within the strutures. The typical size of high-Q modes is smaller than or comparable to the pump spot size, thus the lasing modes correspond to the high-Q modes inside the pump area.

According to the 2D calculation results, the frequencies of the highest-Q modes are the same for polycrystalline and amorphous structures, thus the lasing modes should not shift in frequency as ξ changes. This prediction contradicts the experimental data in Fig. 4, because light leakage in the third dimension is ignored in the calculation of 2D structures. Although light is confined in the free-standing GaAs membrane by index guiding, it can escape from the top or bottom surfaces of the membrane to the surrounding air. To account for this leakage, we performed the three-dimensional (3D) finite-difference time-domain (FDTD) calculation. The structural parameters used in the calculation are identical to those of the fabricated samples.

We calculated the high-Q resonances of TE polarization in the absence of gain or absorption. The quality factors Q_t of all modes within the frequency range of interest were found and plotted versus the normalized frequency a/λ in Fig. 6 for $\xi/a = 2.3$ and 1.4. The values of Q_t are orders of magnitude lower than those in Fig.5(c) for the same value of ξ/a. This result illustrates that the vertical leakage of light is much larger than the lateral leakage for the high-Q resonances. Such strong vertical leakage results from tight confinement in the lateral dimension. Namely, spatial localization of a mode in the xy-plane (parallel to the membrane) results in a broad distribution of in-plane wavevector $\mathbf{k}_{||}$ (projection of $\mathbf{k}$ vector to the xy-plane). The $\mathbf{k}_{||}$ components within the light cone ($|\mathbf{k}_{||}| \leq \omega/c$) can escape from the membrane in the $\pm z$ directions (normal to the membrane). The vertical leakage rate is characterized by the out-of-plane energy loss per optical cycle Q_v^{-1}, and the lateral by Q_h^{-1}. The total loss is described by $Q_t^{-1} = Q_h^{-1} + Q_v^{-1}$.

For the amorphous structure of $\xi/a = 1.4$, the mode of maximal Q_t at $a/\lambda \simeq 0.32$ has $Q_h = 4.88 \times 10^4$, and $Q_v = 1.62 \times 10^3$. Thus, the vertical leakage rate is an order of magnitude larger than the lateral one. In a polycrystalline structure, the tighter in-plane confinement of defect modes within the PBG makes the vertical leakage even stronger. Consequently, the modes at the center of PBG no longer have the highest Q_t, even though their Q_h is maximal. The highest Q_t modes are away from the PBG center, as shown in Fig. 6 for $\xi/a = 2.3$. These modes are less confined in-plane, meaning their Q_h is lower. The larger spread in the xy-plane narrows the $\mathbf{k}_{||}$ distribution. The $\mathbf{k}_{||}$ components within the light cone is reduced, so is the out-of-plane leakage. The maximal-Q_t mode at $a/\lambda = 0.3$ has $Q_h = 7.55 \times 10^4$, and $Q_v = 3.87 \times 10^3$. Although its Q_h is lower than that of the defect modes at $a/\lambda = 0.32$ (PBG center), the Q_v is higher, so is the Q_t. Intuitively, the mode at the higher frequency side of the PBG center, i.e., at $a/\lambda = 0.34$, should have comparable Q_t to the maximal-Q_t mode at the lower frequency side ($a/\lambda = 0.30$), as their spectral distance to the PBG center is the same. However, the Q_t is lower at $a/\lambda = 0.34$, as seen in Fig. 6. This is because the air holes are isolated and the dielectric medium is connected in the membrane. The dielectric band edge at the lower frequency side of PBG is more robust to disorder, as evident in the DOS shown in Fig.5(b). Consequently, light confinement is stronger in the lower frequency part of the PBG, giving higher Q_t at $a/\lambda = 0.3$.

The 3D numerical simulation reveals that the maximal-Q_t modes shift to higher frequency as ξ decreases. This prediction agrees with the experimental observation that the wavelengths of lasing modes decreases from polycrystalline to amorphous patterns.

IV. CONCLUSION

In summary, we demonstrated lasing in photonic polycrystals and amorphous structures. 2D arrays of air holes were fabricated in a free-standing GaAs membrane, and the average size of ordered domains was gradually varied. InAs QDs embedded in the GaAs membrane provide gain under optical pumping. In a photonic polycrystal, defect modes at the center frequency of PBG are tightly confined in-plane, causing strong light leakage out of the plane. The lasing modes move away from the PBG center to reduce the out-of-plane leakage. In a photonic amorphous structure, the depletion of DOS is significantly weakened, and the lasing modes have less in-plane confinement. Nevertheless, the short-range structural order improves optical confinement and enhances the Q factor. The photonic polycrystal laser and amorphous laser are in between the photonic crystal laser and random laser. Understanding their lasing behavior allows to control lasing by varying the degree of structural order.

The authors thank Professor Corey S. O'Hern and Carl Schreck for computer generation of jammed packing of cylinders, and Professors Eric R. Dufresne and Richard O. Prum for useful discussions. This work is funded by NSF Grant No. DMR-0808937 (HC), and a seed grant from the Yale MRSEC (DMR-0520495). J.-K. Yang acknowledges the support of the Basic Science Research Program through the NRF funded by the Korean government (MEST) (2011-0015030). This work also benefited from the facilities and staff of the Yale University Faculty of Arts and

Sciences High Performance Computing Center.

---

[1] J.D. Joannopoulos, S. Johnson, J.Winn, and R.Meade, *Photonic Crystals: Molding the Flow of Light* (Princeton University Press, Princeton, 2008).
[2] C.M. Soukoulis (ed.), *Photonic Crystals and Light Localization in the 21st Century* (Kluwer Academic, Norwell, 2001).
[3] S. Noda and T. Baba (eds.), *Roadmap on Photonic Crystals* (Kluwer Academic, Dordrecht, 2003).
[4] M. Meier, A. Mekis, A. Dodabalapur, A. Timko, R. E. Slusher, J. D. Joannopoulos, and O. Nalamasu, *Appl. Phys. Lett.* **74**, 7 (1999).
[5] H.-G. Park, S.-H. Kim, S.-H. Kwon, Y.-G. Ju, J.-K. Yang, J.-H. Baek, S.-B. Kim, and Y.-H. Lee, *Science* **305**, 1444 (2004).
[6] O. Painter, R. K. Lee, A. Scherer, A. Yariv, J. D. O'Brien, P. D. Dapkus, and I. Kim, *Science* **284**, 1819 (1999).
[7] M. Notomi, H. Suzuki, T. Tamamura, and K. Edagawa, *Phys. Rev. Lett.* **92**, 123906 (2004).
[8] K. Nozaki and T. Baba, *Appl. Phys. Lett.* **84**, 4875 (2004).
[9] S.-K. Kim, J.-H. Lee, S.-H. Kim, I.-K. Hwang, and Y.-H. Lee, *Appl. Phys. Lett.* **86**, 031101 (2005).
[10] K. Nozaki and T. Baba, *Japan. J. Appl. Phys.* **45**, 6087 (2006).
[11] X. Xu, H. Chen, and D. Zhang, *Appl. Phys. B* **89**, 29 (2007).
[12] C. Jin, X. Meng, B. Cheng, Z. Li, and D. Zhang, *Phys. Rev. B* **63**, 195107 (2001).
[13] J. Ballato, J. Dimaio, A. James, and E. Gulliver, *Appl. Phys. Lett.* **75**, 1497 (1999).
[14] C. Rockstuhl, U. Peschel, and F. Lederer, *Opt. Lett.* **31**, 1741 (2006).
[15] Y. Wang and S. Jian, *Phys. Lett. A* **352**, 550 (2006).
[16] C. Rockstuhl and F. Lederer, *Phys. Rev. B* **79**, 132202 (2009).
[17] P. D. García, R. Sapienza, Á. Blanco, and C. López, *Adv. Mater.* **19**, 2597 (2007).
[18] K. Edagawa, S. Kanoko, and M. Notomi, *Phys. Rev. Lett.* **100**, 013901 (2008).
[19] M. Florescu, S. Torquato, and P. Steinhardt, *Proc. Nat. Aca. Sci. Am.* **106**, 20658 (2009).
[20] J.-K. Yang, C. Schreck, H. Noh, S.-F. Liew, M. I. Guy, C. S. O'Hern, and H. Cao, *Phys. Rev. A* **82**, 053838 (2010).
[21] H. Noh, J.-K. Yang, S. F. Liew, M. J. Rooks, G. S. Solomon, and H. Cao, *Phys. Rev. Lett.* **106**, 183901 (2011).
[22] G. Pompe, T. Rappen, M. Wehner, F. Knop, and M. Wegerner, *Phys. Stat. Sol. (b)* **188**, 175 (1995).
[23] F. Jahnke and S. W. Koch, *Phys. Rev. A* **52**, 1712 (1995).
[24] J. B. Pendry, *J. Phys. C* **20**, 733 (1987); J. B. Pendry, *Adv. Phys.* **43**, 461 (1994).
[25] C. Vanneste and P. Sebbah, *Phys. Rev. A* **79**, 041802 (2009).
[26] S. G. Johnson and J. D. Joannopoulos, *Opt. Express* **8**, 173 (2001).
[27] J. Andreasen, C. Vanneste, L. Ge, and H. Cao, *Phys. Rev. A* **81**, 043818 (2010).
[28] S. F. Liew, J. Forster, H. Noh, C. F. Schreck, V. Saranathan, X. Lu, L. Yang, R. O. Prum, C. S. OHern, E. R. Dufresne, and H. Cao, *Opt. Express* **19**, 8208 (2011).
[29] J. Andreasen and H. Cao, *Opt. Lett.* **34**, 3586 (2009).
[30] X. Wu, J. Andreasen, H. Cao, and A. Yamilov, *J. Opt. Soc. Am. B* **24**, A26 (2007).